Check for updates

The effect of rare earth modification on the denitration performance of Fe$_2$O$_3$–MnO$_2$/TiO$_2$ catalysts

Yuming Yang, [ID] [abc] Xue Bian, [ID] *[c] Jiaqi Li,[ab] Zhongshuai Jia[ab] and Yuting Bai[d]

High denitration efficiency and strong adaptability to flue gas temperature fluctuations are essential properties for NH$_3$ selective catalytic reduction (SCR) catalysts. In this study, rare earth oxide modification of the catalyst 8Fe$_2$O$_3$–40MnO$_2$/TiO$_2$ via the addition of CeO$_2$ during the preparation process is explored. The results show that the 8Fe$_2$O$_3$–6CeO$_2$–40MnO$_2$/TiO$_2$ catalyst has excellent denitration properties, with a denitration efficiency of greater than 90%. The operational temperature range reaches 129 to 390 °C, and its N$_2$ selectivity, anti-SO$_2$ performance and anti-H$_2$O performance are good, with the denitration performance being significantly improved. The addition of 6% CeO$_2$ promotes the lattice shrinkage of TiO$_2$, improves its dispersion, refines the grain size, and increases the specific surface area of the catalyst. At the same time, CeO$_2$ increases the chemical adsorption of oxygen on the catalyst surface and the proportion of low-valence metal ions, promotes electron transfer between active elements, generates more surface reactive oxygen species, and increases the content of oxygen vacancies and adsorption sites for NO$_x$ and NH$_3$. It also significantly improves the redox performance of the catalyst, which is especially conducive to the generation of weak and medium-strong acidic sites on the catalyst surface. The NH$_3$-SCR reaction on the surface of the 8Fe$_2$O$_3$–6CeO$_2$–40MnO$_2$/TiO$_2$ catalyst follows both L–H and E–R mechanisms, with the L–H mechanism being dominant.

1 Introduction

Nitrogen oxide (NO$_x$) pollutants have become one of the main sources of air pollution. Among industrial NO$_x$ emission sources, the power industry accounts for the largest proportion.[1,2] Excessive NO$_x$ in the atmosphere can lead to disasters such as acid rain, photochemical smog, eutrophication of water bodies, and the greenhouse effect.[3] In recent years, China's regulations on industrial NO$_x$ emissions have become increasingly stringent, placing significant environmental pressure on metallurgical, building materials, glass, and other industrial enterprises. The selective catalytic reduction (SCR) method is currently the most widely used flue gas denitration technology for controlling NO$_x$ emissions from industrial sources.[4] The most mature catalyst for this method is V$_2$O$_5$-WO$_3$(MoO$_3$)/TiO$_2$, which belongs to the category of medium-temperature catalysts.[5] To avoid SO$_2$ poisoning, the V$_2$O$_5$-WO$_3$(MoO$_3$)/TiO$_2$ catalyst is placed after the desulfurization and dust removal

units in the flue gas treatment process. As a result, the flue gas must be reheated before denitration, which imposes greater economic pressure on enterprises. The vanadium component in the catalyst is toxic, and the disposal and recycling of waste catalyst can easily cause environmental pollution. Therefore, non-toxic SCR catalysts capable of denitration at low temperatures have broad application prospects.

Among the many transition metal oxides, MnO$_x$ has the advantages of multivalent states, strong acidity, and low cost. Fe$_2$O$_3$ can further expand the active temperature range of the SCR catalyst. Therefore, low-temperature SCR denitration catalysts with MnO$_x$ and Fe$_2$O$_3$ as the main active components or additives have become research hotspots in the field of denitration catalysts.[6] Liu et al.[7] used the sol–gel method to prepare a series of Mn–Ti oxide catalysts. Through experiments, it was found that such catalysts exhibit high low-temperature SCR activity. This excellent low-temperature NH$_3$-SCR activity can be attributed to their appropriate structural properties, amorphous manganese oxides with equal proportions of Mn^{3+}/Mn^{4+}, good low-temperature reducibility, and abundant surface acidic sites. Mu et al.[8] prepared a Fe$_2$O$_3$–MnO$_2$/TiO$_2$ catalyst using an ethylene-glycol-assisted impregnation method; the catalyst showed excellent low-temperature activity, a low apparent activation energy, and strong resistance to sulfur poisoning. Characterization results indicate that the catalyst has high dispersion, small particle size, and partial doping of Fe into the

[a]Mining Research Institute of Baotou Steel (Group) Corp., Baotou 014030, China

[b]Inner Mongolia Key Laboratory of Mining and Metallurgical Solid Waste Resource and Green Comprehensive Utilization, Baotou 014030, China

[c]School of Metallurgy, Northeastern University, Shenyang 110819, China. E-mail: bianx@smm.neu.edu.cn

[d]School of Metallurgy and Materials Engineering, Liaoning Institute of Science and Technology, Benxi 117004, China

TiO_2 lattice to form a Fe–O–Ti structure, which enhances the electronic inductive effect and increases the proportion of surface-chemisorbed oxygen. The NO oxidation is thus enhanced through the "fast SCR" process, which is conducive to low-temperature SCR activity.

China is the country with the richest rare earth ore resources in the world.[9] The combination of rare earth oxides with other metal oxides for the research and development of denitration catalysts can achieve efficient denitration of industrial flue gas at a low cost; this catalyst preparation technology route is in alignment with China's national conditions. Many studies have shown that rare earth modification can improve the denitration performance and sulfur resistance of SCR catalysts. Zhai *et al.*[10] used the coprecipitation method to modify an MnO_x catalyst with Pr and found that the Pr-modified MnO_x catalyst had significantly improved tolerance to SO_2. The characterization results showed that the Pr-modification of the MnO_x catalyst improves the specific surface area, dispersion, reducibility, surface Mn^{4+} content, and relative percentage of chemically adsorbed oxygen (O_α) of the catalyst. Additionally, Pr modification increases the adsorption of NH_3 on the surface of the catalyst, resulting in more Lewis acidic sites on the surface of the $MnPrO_x$-0.1 catalyst. These factors contributed to the good catalytic properties of the Pr-modified MnO_x catalyst. Research by Liu *et al.*[11] found that the addition of Ce can promote the dispersion of MnO_x on the TiO_2 carrier. Doping Ce into MnO_x can also increase the content of Mn^{4+} species. These species play a vital role in the NO oxidation reaction, which can trigger the "fast SCR" reaction and promote the conversion of NO_x. Gao *et al.*[12] found that the introduction of Sm can effectively inhibit the crystallization process of MnO_x and TiO_2, increase the specific surface area, enhance the surface concentration of chemically adsorbed oxygen, and increase the number of strong acid sites on the surface, thereby optimizing the catalytic performance of the catalyst. Huang *et al.*[13] added 3% of a rare earth element (Nd) to a 30% Mn/TiO_2 catalyst to improve its low-temperature catalytic performance. The addition of Nd increases the specific surface area of the catalyst, decreases the average pore size, and enhances the dispersion of MnO_x, which are the main reasons for the enhanced catalytic activity.

Through previous research and early experimental demonstrations by this group, it has been concluded that the denitration performance of the Fe_2O_3–MnO_2/TiO_2 catalyst is superior when MnO_2 and Fe_2O_3 account for 0.4 and 0.08 of the overall mass of the catalyst, respectively.[8] CeO_2 exhibits acidity, which can enhance the surface acidity and redox properties of the catalyst.[14,15] At the same time, the interactions among Ce, Mn, and Fe are helpful in increasing the number of active sites of the catalyst and improving the dispersion state of the active components on the carrier.[16,17] In order to clarify the mechanism by which CeO_2 modification influences the denitration performance of the catalyst $8Fe_2O_3$–$40MnO_2/TiO_2$, this study employs XRD, BET, XPS, SEM, TEM, H_2-TPR, NH_3-TPD, and *in situ* DRIFTS to investigate the effects of modification with CeO_2 on the denitration performance, catalytic material morphology, surface acidity, redox capacity, and catalytic mechanisms of the $8Fe_2O_3$–$40MnO_2/TiO_2$ catalyst. This study aims to provide

theoretical and technical support for the research, development, and application of rare-earth-modified denitration catalysts.

2 Materials and methods

2.1 Catalyst preparation

The Fe_2O_3–CeO_2–MnO_2/TiO_2 catalyst was prepared by the co-precipitation method. The preparation steps were as follows: manganese acetate tetrahydrate (($CH_3COO)_2Mn\cdot4H_2O$), cerium chloride heptahydrate ($CeCl_3\cdot7H_2O$), iron chloride hexahydrate ($FeCl_3\cdot6H_2O$), and anatase (TiO_2) were added to a beaker containing deionized water in a specific weight ratio. The mixture was continuously stirred for 0.5 hours, and ammonia was then added dropwise to the catalyst solution until the pH reached 9–10. After that, the mixture was stirred for an additional 3 hours and then filtered, and deionized water was added to the filter cake. The mixture was stirred and washed for 0.5 hours and then filtered again. These operations were repeated three times. The resulting filter cake was dried at 75 °C for 24 hours. Finally, the dried filter cake was placed in a muffle furnace and calcined for a certain period of time to obtain the $8Fe_2O_3$–$yCeO_2$–$40MnO_2/TiO_2$ catalyst. The value y represents the mass percentage of CeO_2 in the entire catalyst ($\times100$), and the values used were 0, 3, 6, and 9. The actual y values were determined by ICP and rounded to the nearest integer. The preparation process is shown in Fig. 1.

2.2 Catalyst characterization

X-ray diffraction (XRD) analysis was conducted using an X-ray diffractometer, model JSM-7800F, manufactured by the Japanese Electronics Company. The test conditions included a Cu target, Kα radiation, an analysis voltage of 40 kV, an analysis current of 40 mA, a scanning range of 5° to 90°, and a scanning rate of 2° per minute.

The N_2 adsorption–desorption curve was measured using an ASAP-2020 physical adsorption instrument from Micromeritics Company in the United States. Prior to the test, the sample was vacuum treated at 400 °C for 4 hours. The Brunauer–Emmett–Teller (BET) method was used to calculate the specific surface area of the sample, and the Barrett–Joyner–Halenda (BJH) method was employed to determine the pore size distribution.

For scanning electron microscope (SEM) analysis, a Hitachi SU8020 ultra-high-resolution field emission scanning electron microscope was used, with a magnification range from 300 000× to 800 000×. The X-ray spectrometer attached to the SEM has an elemental analysis range from B5 to U92 and an energy resolution of 130 eV.

A JEM-2100F transmission electron microscope (TEM, Japan) was used, which has a point resolution of 0.23 nm, a magnification range of 50 to 1 000 000, and an acceleration voltage of 200 kV. Using this instrument, we observed the particle size and microstructure of the catalyst and conducted nanoscale analysis of the catalyst through high-resolution lattice fringe images.

X-ray photoelectron spectroscopy (XPS) was carried out using the Thermo Fisher Scientific Escalab 250Xi X-ray Photoelectron
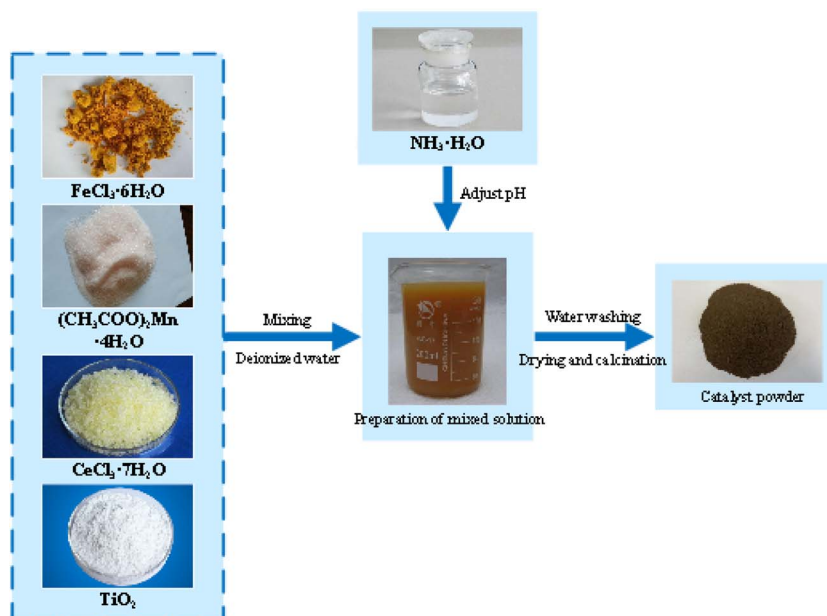
Fig. 1 The $8Fe_2O_3-yCeO_2-40MnO_2/TiO_2$ catalyst preparation process.

Spectrometer. The excitation source was Al Kα (1486.6 eV), and the acceleration voltage was 150 W. The binding energy of C 1s (284.8 eV) was used as the internal standard. Peak fitting was performed using XPS Peak software.

Temperature-programmed reduction (TPR) analysis was conducted using a Micromeritics Autochem II 2920 chemical adsorption instrument (USA). The test conditions were as follows: approximately 70 mg of the sample was placed in a quartz tube, heated to 300 °C for drying and pretreatment, purified with He gas for 1 hour, and then cooled to room temperature. A 10% H_2/Ar mixture was passed through it for 30 minutes until the baseline was stable. Finally, it was heated to 800 °C in a 10% H_2/Ar atmosphere for TPR. The gas flow rate was 50 mL min^{-1}, and the heating rate was 10°C min^{-1}. The detector used was a thermal conductivity detector (TCD), which detects the consumption of the reducing gas.

Temperature-programmed desorption (TPD) tests were carried out on an AutoChem II 2920 Chemisorption Analyzer. The specific conditions were as follows: approximately 70 mg of the sample was weighed out and placed into a quartz tube; the sample was then heated to 300 °C for drying and pretreatment under a flowing He gas atmosphere. After 1 hour, it was cooled to room temperature. Subsequently, a 10% NH_3/He gas mixture was introduced for 1 hour to achieve saturation; the gas was then switched to He, and the sample was purged for 1 hour to remove physically adsorbed NH_3. Finally, the sample was heated to 800 °C at a rate of 10 °C min^{-1} under a He gas flow (50 mL min^{-1}), and the desorbed gas was detected using a TCD.

In situ diffuse reflectance infrared Fourier transform spectroscopy (*in situ* DRIFTS) was performed using a Thermo Scientific Nicolet IS50 Fourier Transform Infrared (FTIR) spectrometer. The measurement procedure was as follows: approximately 15 mg of sample was placed flat in a small crucible and fixed inside a high-temperature *in situ* cell. The sample was pretreated with N_2 at 400 °C for 1 hour, then cooled to room temperature. Background spectra (32 scans, 4 cm^{-1} resolution) were collected periodically as references. Subsequently, the corresponding reaction gas (1000 ppm NH_3, 1000 ppm NO, and 5% O_2 by volume) was introduced for *in situ* infrared adsorption studies. For NH_3 or NO + O_2 adsorption, the gas was introduced at 200 °C, and data were collected over time. For the experiment involving initial NH_3 pre-adsorption followed by NO + O_2 exposure, saturated NH_3 adsorption was first conducted at 200 °C, after which the NO + O_2 mixture was introduced, and data were collected over time. Similarly, for the experiment involving initial NO + O_2 pre-adsorption followed by NH_3 exposure, saturated NO + O_2 adsorption was performed at 200 °C, followed by NH_3 introduction, and data were collected over time. At the end, the background spectrum was subtracted to obtain the infrared spectra at each time point.

2.3 Measurement of catalyst activity

The laboratory micro-reaction device shown in Fig. 2 was used to simulate the components of flue gas. The test conditions were as follows: a 5 mL catalyst sample, a gas hourly space velocity (GHSV) of 36 000 h^{-1}, and a simulated flue gas composition consisting of 600 ppm NO, 300 ppm O_2, 600 ppm NH_3, and 60 ppm SO_2 (when required), with N_2 as the balance gas. Five milliliters of the catalyst to be tested were placed in a fixed-bed reactor, the flow control system was turned on, and the gas parameters were set. The pipeline was purged with N_2, and the air-tightness of the system was checked after 5 minutes. Then, the final temperature was set, the temperature control switch was turned on, other gases were introduced, and the NO concentration detected by the analyzer was recorded as the temperature changed. After the test was completed, the other
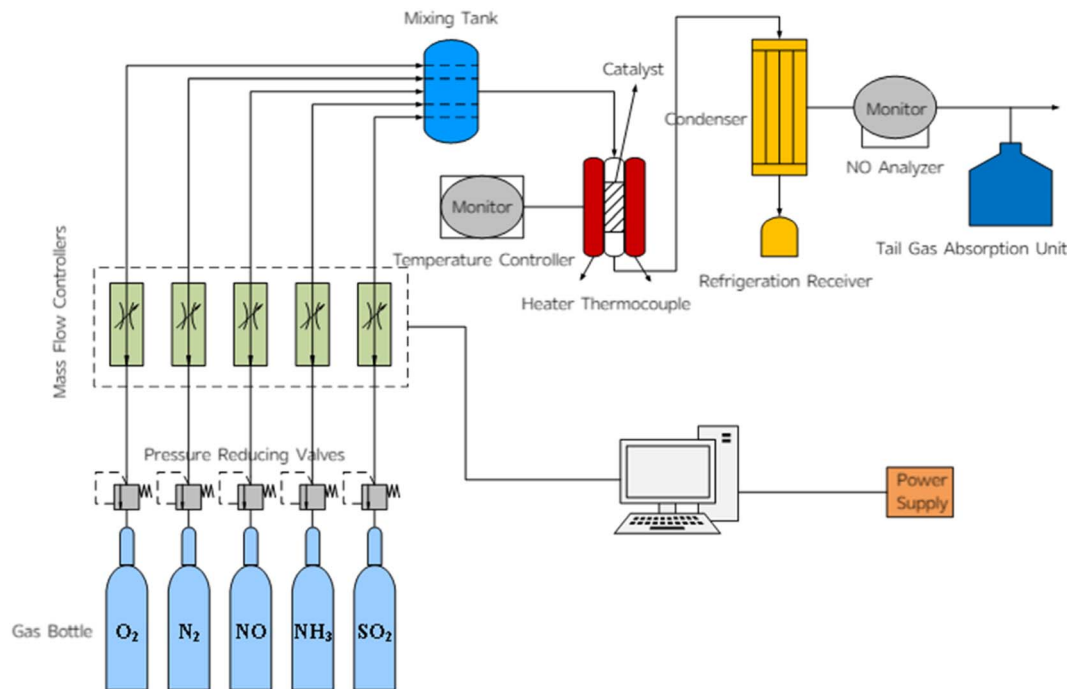
Fig. 2 A schematic diagram of the fixed-bed catalytic reactor.

gas switches were turned off, N_2 continued to flow, and the pipeline was purged with N_2 until the NO detection indicator dropped to zero.

The equations for calculating the denitration efficiency and N_2 selectivity of the catalyst are as follows:

$$\text{NO conversion} = \frac{[NO]_{in} - [NO]_{out}}{[NO]_{in}} \times 100\% \qquad (2.1)$$

$$N_2 \text{ selectivity} = \left[1 - \frac{2[N_2O]}{[NH_3]_{in} - [NH_3]_{out} + [NO]_{in} - [NO]_{out}}\right] \\ \times 100\% \qquad (2.2)$$

where $[NO]_{in}$ represents the input concentration of NO, $[NO]_{out}$ denotes the output concentration of NO, $[NH_3]_{in}$ signifies the input concentration of NH_3, $[NH_3]_{out}$ refers to the output concentration of NH_3, and $[N_2O]$ is the output concentration of N_2O.

3 Results and discussion

3.1 Morphology and structure of the catalysts

3.1.1 XRD, BET surface area and pore morphology.
The phase composition analysis results for the $8Fe_2O_3-yCeO_2-40MnO_2/TiO_2$ catalyst are shown in Fig. 3.

The characteristic peaks of the catalyst in the figure are mainly the diffraction peaks of anatase TiO_2 and MnO_2. There are no obvious Fe_2O_3 or CeO_2 diffraction peaks, indicating that these form an amorphous structure or are evenly distributed on the surface of the support. According to the Bragg equation, $2d \sin\theta = n\lambda$ (where d is the lattice spacing, θ represents the diffraction angle, n denotes the reflection series, and λ is the wavelength), the diffraction angle is inversely proportional to the lattice spacing of the crystal. As the CeO_2 content increases, the TiO_2 diffraction peak at $25.3°$ shifts toward higher angle. The $8Fe_2O_3-6CeO_2-40MnO_2/TiO_2$ catalyst exhibits the largest shift and the lowest intensity at $25.3°$. At this point, the unit cell parameters of TiO_2 in the catalyst are the smallest. The lattice spacing of TiO_2 in each catalyst is listed in Table 1. As the CeO_2 content increases from 0% to 6%, the lattice spacing of TiO_2 decreases from 0.351 nm to 0.345 nm. With further increase of the CeO_2 content, the lattice spacing of TiO_2 no longer decreases, indicating that an appropriate amount of amorphous CeO_2 inhibits the lattice expansion of the TiO_2 support and enhances the dispersion of TiO_2. At the same time, the low intensity of the MnO_2 diffraction peak may be due to interaction between CeO_2 and MnO_2 that reduces the crystallinity of MnO_2 and increases its dispersion on the surface of the catalyst. The improved dispersion of the active components can provide better mass transfer and diffusion properties, which helps to accelerate the acid cycle and the redox cycle.[18]

The NH_3-SCR reaction mainly occurs on the surface of the catalyst. Micropores and mesopores can provide a larger internal surface area and pore volume during the SCR reaction, resulting in a higher BET surface area, which is conducive to improving the denitration performance of the catalyst.[19] Therefore, in this study, the pore structure characteristics of the $8Fe_2O_3-yCeO_2-40MnO_2/TiO_2$ catalyst were tested using the N_2 adsorption–desorption measurement method, and the results are shown in Table 1. The specific surface area and pore capacity of the $8Fe_2O_3-40MnO_2/TiO_2$ catalyst are the smallest, at $84.13~m^2~g^{-1}$ and $0.222~cm^3~g^{-1}$, respectively. As the CeO_2
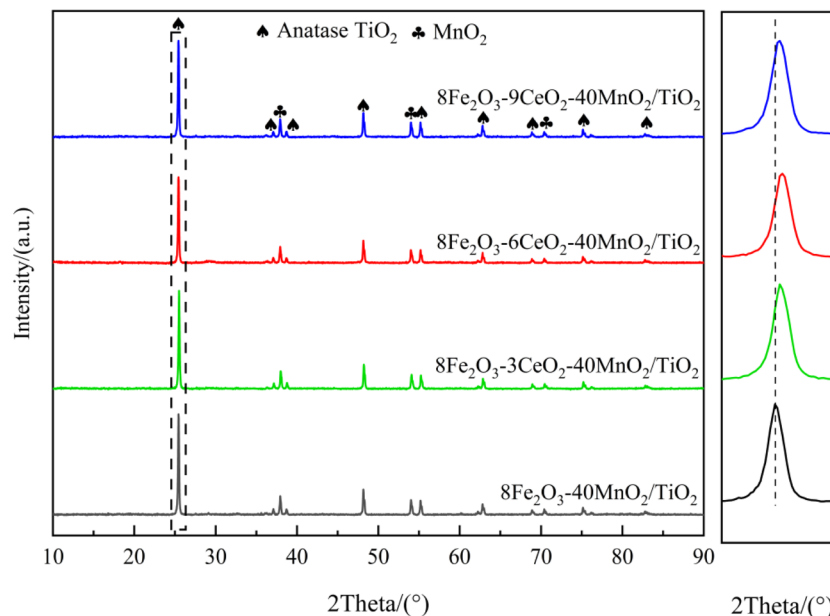
Fig. 3 XRD diffraction patterns of the $8Fe_2O_3-yCeO_2-40MnO_2/TiO_2$ catalysts.

Table 1 Specific surface area and pore size parameters of the $8Fe_2O_3-yCeO_2-40MnO_2/TiO_2$ catalysts

Catalyst	Specific surface area/m^2 g^{-1}	Pore capacity/ cm^3 g^{-1}	Pore size/ nm	TiO$_2$ (101) crystal plane spacing/nm
$8Fe_2O_3-40MnO_2/TiO_2$	84.13	0.222	15.36	0.351
$8Fe_2O_3-3CeO_2-40MnO_2/TiO_2$	85.26	0.243	13.59	0.349
$8Fe_2O_3-6CeO_2-40MnO_2/TiO_2$	87.73	0.268	12.22	0.345
$8Fe_2O_3-9CeO_2-40MnO_2/TiO_2$	87.48	0.259	12.47	0.346

content increases, the specific surface area and pore capacity of the catalyst gradually increase, while the average pore size decreases. This phenomenon indicates that more microporous structures are formed on the surface of the catalyst, which is conducive to providing more active sites and adsorbing more NH$_3$. The specific surface area (87.73 m^2 g^{-1}) and pore capacity (0.268 cm^3 g^{-1}) of the $8Fe_2O_3-6CeO_2-40MnO_2/TiO_2$ catalyst are the largest, and its average pore size (12.22 nm) is the smallest. The main reason is that an appropriate amount of CeO$_2$ inhibits the growth of the TiO$_2$ support crystal particles, thereby increasing the specific surface area and pore capacity of the catalyst, which is consistent with the XRD results.

3.1.2 Morphological analysis. The SEM image of the $8Fe_2O_3-yCeO_2-40MnO_2/TiO_2$ catalyst is presented in Fig. 4.

It can be seen from Fig. 4 that the catalyst mainly exists in the form of particles with uneven sizes, and these particles exhibit varying degrees of agglomeration. In Fig. 4(a), it can be clearly observed that the $8Fe_2O_3-40MnO_2/TiO_2$ catalyst has a higher content of coarse particles, a more uneven particle size distribution, and a more severe agglomeration phenomenon. As the CeO$_2$ content increases, the agglomeration of the catalyst particles gradually decreases. Fig. 4(c) shows that the $8Fe_2O_3-6CeO_2-40MnO_2/TiO_2$ catalyst has a more uniform particle size and less agglomeration compared to the other catalysts,

indicating that it can provide more active and reactive sites for the denitration reaction. This is consistent with the denitration performance test results presented in Section 3.6. Fig. 4(d) shows that further increasing the CeO$_2$ content inhibits the dispersion of catalyst particles, resulting in an increase in surface aggregation.

The TEM images of the $8Fe_2O_3-yCeO_2-40MnO_2/TiO_2$ catalyst are shown in Fig. 5. Most of the catalysts exist as particles of different sizes, and the dark fine particles are generally adsorbed on the surface of the coarse particles (*i.e.*, the TiO$_2$ carrier). Most of the TiO$_2$ grain sizes in Fig. 5 are between 10 and 50 nm. As the CeO$_2$ content increases, the TiO$_2$ grain size tends to decrease, indicating that the addition of CeO$_2$ can inhibit the growth of TiO$_2$ grains, which is consistent with the XRD analysis results. At the same time, with increasing CeO$_2$ content, the number of fine particles the of active substances loaded on the surface of the carrier increases, and their distribution gradually becomes denser and more uniform. The number of active substance particles exposed on the surface of the $8Fe_2O_3-6CeO_2-40MnO_2/TiO_2$ catalyst was significantly increased, which provides more active reaction sites for the catalytic reaction and is conducive to promoting the NH$_3$-SCR reaction.

Fig. 6 presents the high-resolution lattice fringe images of the $8Fe_2O_3-yCeO_2-40MnO_2/TiO_2$ catalysts. In the figure, the
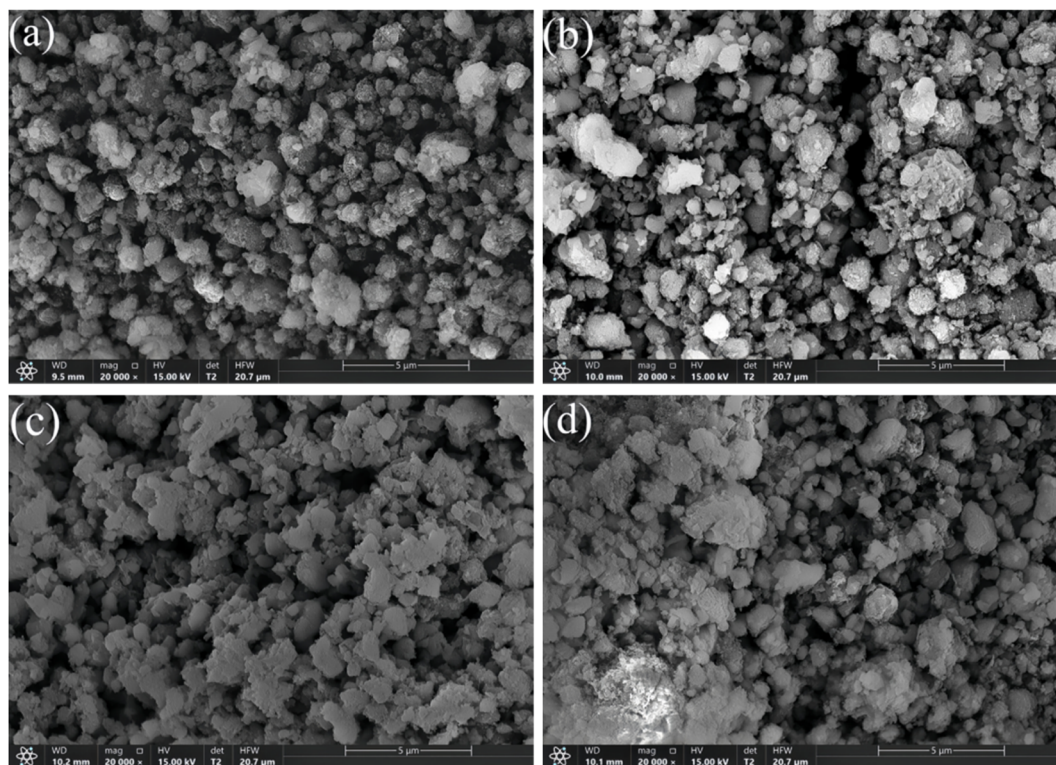
Fig. 4 SEM images of the $8Fe_2O_3-yCeO_2-40MnO_2/TiO_2$ catalysts: (a) $8Fe_2O_3-40MnO_2/TiO_2$; (b) $8Fe_2O_3-3CeO_2-40MnO_2/TiO_2$; (c) $8Fe_2O_3-6CeO_2-40MnO_2/TiO_2$; and (d) $8Fe_2O_3-9CeO_2-40MnO_2/TiO_2$.

lattice fringe spacings of approximately $d = 0.351$ nm correspond to the TiO_2 (101) crystal plane, while lattice fringe spacings of $d = 0.236$ nm and $d = 0.287$ nm correspond to the MnO_2 (004) and MnO_2 (200) crystal planes, respectively. As the CeO_2 content increases, the lattice fringe spacing corresponding to the TiO_2 (101) crystal plane gradually decreases, indicating that an increase in CeO_2 content can inhibit the crystal growth of TiO_2, which is consistent with the XRD analysis results mentioned above. Additionally, no lattice fringes associated with Fe_2O_3 or CeO_2 are observed in the figure, suggesting that the active components Fe_2O_3 and CeO_2 may exist in the catalyst in the form of a solid solution, while MnO_2 is evenly dispersed on the surface of the TiO_2 support in the form of fine particles. This is consistent with the XRD results, in which the diffraction peaks of Fe_2O_3 and CeO_2 disappeared, and only the characteristic diffraction peaks of TiO_2 and MnO_2 were present.

3.2 Surface properties of the catalysts

In order to explore the influence of the addition of CeO_2 on the surface elemental distribution and redox performance of the $8Fe_2O_3-yCeO_2-40MnO_2/TiO_2$ catalyst, XPS tests were performed on catalysts prepared using different amounts of CeO_2, and the results are shown in Fig. 7 and Table 2.

Fig. 7(a) shows the O 1s spectrum of the $8Fe_2O_3-yCeO_2-40MnO_2/TiO_2$ catalysts. Two characteristic peaks located around 532.2 eV and 530.1 eV appear in the figure, which correspond to the chemisorbed oxygen O_α and lattice oxygen O_β, respectively. As the amount of CeO_2 added was increased, the ratio of O_α to the total oxygen ($O_\alpha/(O_\alpha + O_\beta)$) on the catalyst surface gradually increased. As presented in Table 2, the total amount of surface oxygen changed relatively little, indicating that part of the O_β was converted to O_α as the amount of CeO_2 added was increased. Since O_α has a higher mobility than O_β, it is more active, and the increase in the proportion of O_α is conducive to NO oxidation and the subsequent "fast SCR" reaction.[20] The maximum $O_\alpha/(O_\alpha + O_\beta)$ value of 45.7% was achieved by the $8Fe_2O_3-6CeO_2-40MnO_2/TiO_2$ catalyst surface. The main reason is that as amount of CeO_2 increases, the Ce^{3+} content on the catalyst surface increases, causing the catalyst surface to produce more oxygen vacancies and O_α.

Fig. 7(b) and (d) show the Mn 2p and Fe 2p profiles of the $8Fe_2O_3-yCeO_2-40MnO_2/TiO_2$ catalysts, respectively. As the amount of CeO_2 was changed, the position of each of the characteristic peaks and the peak areas remained relatively constant. That is, the ratios of Fe^{2+}/Fe^{3+} and Mn^{3+}/Mn^{4+} on the catalyst surface did not change significantly, indicating that the variation in the amount of CeO_2 added did not cause a major change in the valence states of the elements Mn and Fe on the surface of the catalyst.

The Ce 3d map of the $8Fe_2O_3-yCeO_2-40MnO_2/TiO_2$ catalyst is shown in Fig. 7(c). The Ce 3d orbital includes the Ce $3d_{3/2}$ spin–orbit component (u) and the Ce $3d_{5/2}$ spin–orbit component (v). The Ce species on the surface of the catalyst mainly exist in the form of Ce_2O_3 and CeO_2. The peaks u′ and v′ in the figure correspond to Ce^{3+}, and the peaks u, u″, u‴, and v, v″, and v‴ belong to Ce^{4+}. It can be found that as the amount of CeO_2
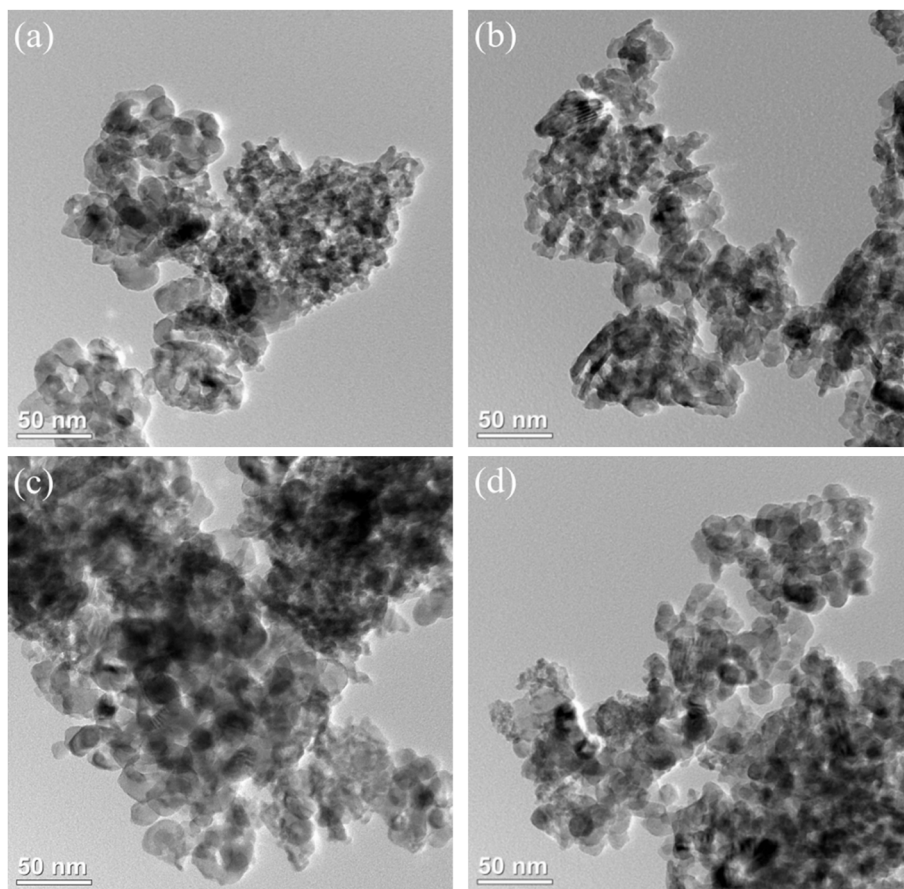
Fig. 5 TEM images of the $8Fe_2O_3-yCeO_2-40MnO_2/TiO_2$ catalysts: (a) $8Fe_2O_3-40MnO_2/TiO_2$; (b) $8Fe_2O_3-3CeO_2-40MnO_2/TiO_2$; (c) $8Fe_2O_3-6CeO_2-40MnO_2/TiO_2$; and (d) $8Fe_2O_3-9CeO_2-40MnO_2/TiO_2$.
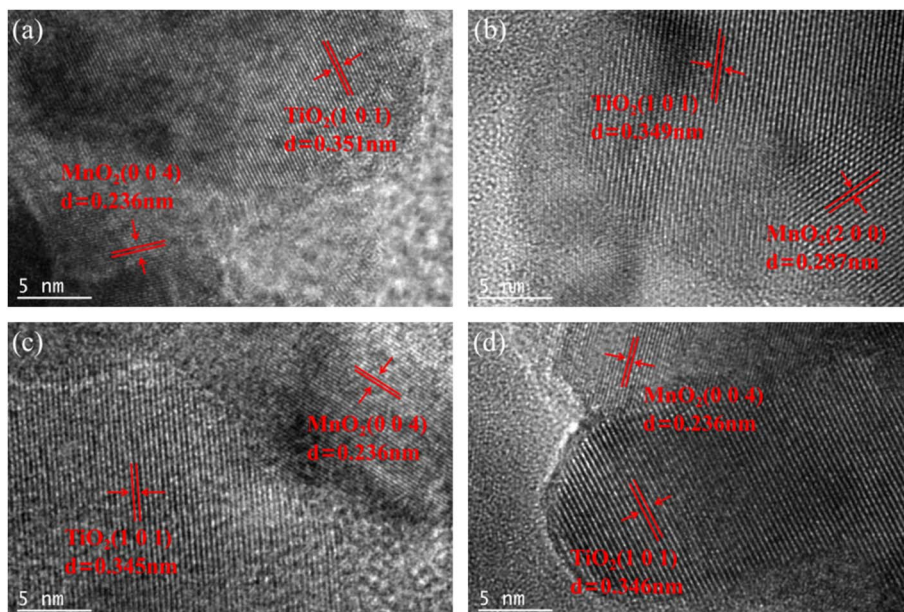
Fig. 6 Lattice fringe patterns of the $8Fe_2O_3-yCeO_2-40MnO_2/TiO_2$ catalysts: (a) $8Fe_2O_3-40MnO_2/TiO_2$; (b) $8Fe_2O_3-3CeO_2-40MnO_2/TiO_2$; (c) $8Fe_2O_3-6CeO_2-40MnO_2/TiO_2$; and (d) $8Fe_2O_3-9CeO_2-40MnO_2/TiO_2$.
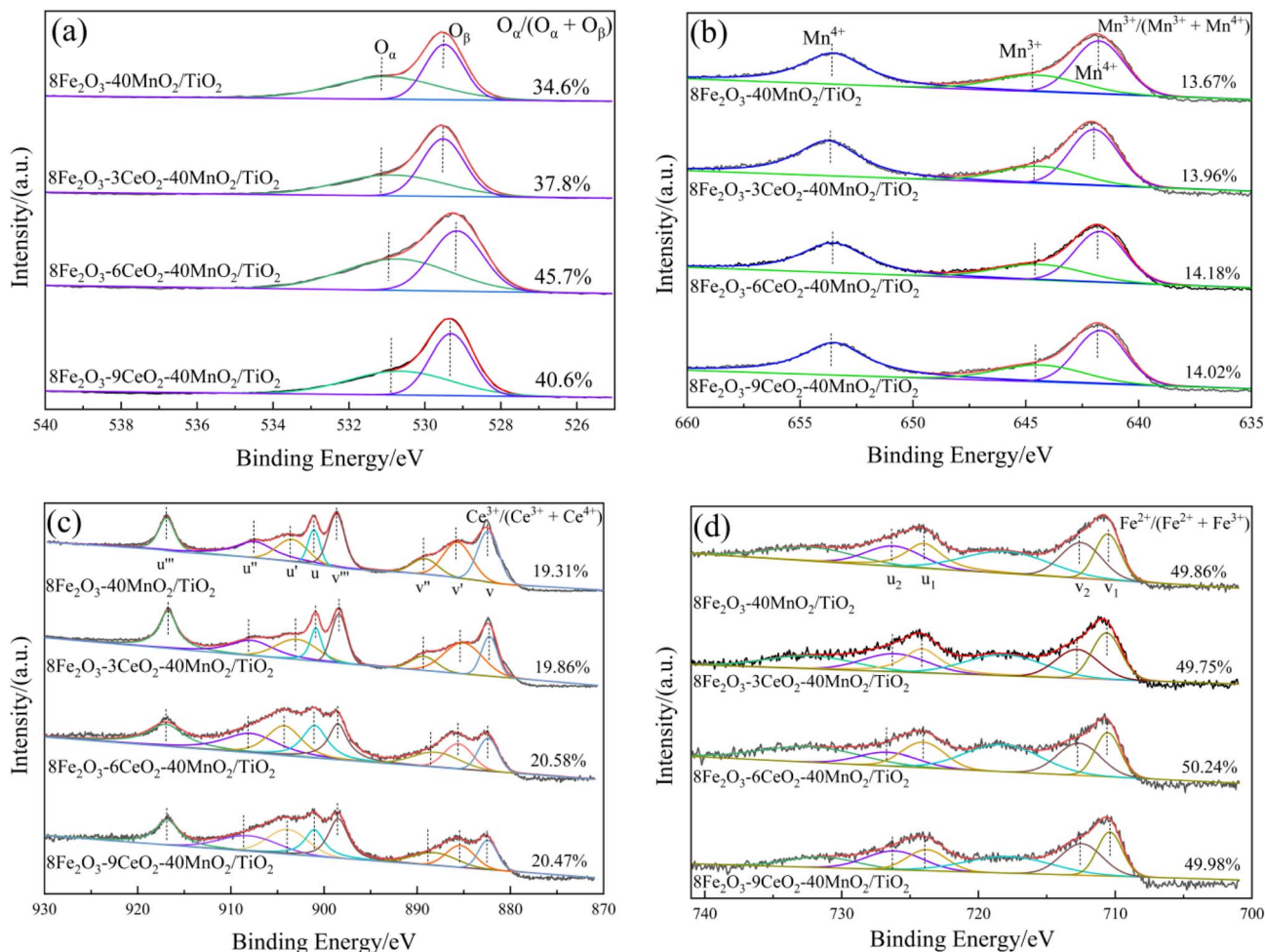
Fig. 7 XPS spectra of the $8Fe_2O_3–yCeO_2–40MnO_2/TiO_2$ catalysts: (a) O 1s; (b) Mn 2p; (c) Ce 3d; and (d) Fe 2p.

Table 2 Surface element content of the $8Fe_2O_3–yCeO_2–40MnO_2/TiO_2$ catalysts (mass%)

Catalyst	Fe	Ce	Mn	Ti	O
$8Fe_2O_3–40MnO_2/TiO_2$	6.37	1.53	11.72	12.34	68.04
$8Fe_2O_3–3CeO_2–40MnO_2/TiO_2$	5.46	3.24	11.07	11.36	68.87
$8Fe_2O_3–6CeO_2–40MnO_2/TiO_2$	4.96	4.51	9.98	10.30	70.25
$8Fe_2O_3–9CeO_2–40MnO_2/TiO_2$	5.03	5.65	9.35	10.84	69.13

increases, the ratio of Ce^{3+} to total Ce ($Ce^{3+}/(Ce^{3+} + Ce^{4+})$) on the catalyst surface also increases, and the proportion of Ce^{3+} on the catalyst surface of $8Fe_2O_3–6CeO_2–40MnO_2/TiO_2$ reaches 20.58%, indicating that increasing addition of CeO_2 promotes the forward reaction: $Ce^{4+} \leftrightarrow Ce^{3+} + Cat–[O]$. Studies have shown that the presence of Ce^{3+} on the surface of the catalyst is conducive to improving its catalytic performance, because the Ce^{3+}/Ce^{4+} redox cycling can generate charge imbalance, oxygen vacancies, and unsaturated chemical bonds, among others.[21] Therefore, a higher proportion of Ce^{3+} can increase the number of active sites on the surface of the catalyst and enhance its redox performance.

3.3 Raman spectroscopic analysis of the catalysts

In metal oxides, the formation of oxygen vacancies reduces the symmetry of the crystal structure, thereby affecting the Raman spectrum. Raman spectral characterization was performed on the $8Fe_2O_3–yCeO_2–40MnO_2/TiO_2$ catalysts with different amounts of added CeO_2, and the results are shown in Fig. 8. The characteristic peak at 148 cm^{-1} corresponds to the vibration of the Ti–O bond in anatase TiO_2, while the characteristic peaks at 393 cm^{-1}, 509 cm^{-1}, and 642 cm^{-1} correspond to CeO_2, MnO_2, and Fe_2O_3, respectively. As the amount of CeO_2 added increases, the intensity of the characteristic peak at 393 cm^{-1} gradually increases, and the intensity of the characteristic peak at 148 cm^{-1} also changes significantly. The intensity of the characteristic Ti–O bond peak of the $8Fe_2O_3–6CeO_2–40MnO_2/TiO_2$ catalyst increases significantly, indicating that with the addition of 6% CeO_2, the number of oxygen vacancies on the catalyst surface increases. Combined with the previous XPS detection results, this indicates that an increase in the ratio of Ce^{3+} can promote an increase in oxygen vacancies on the catalyst surface.
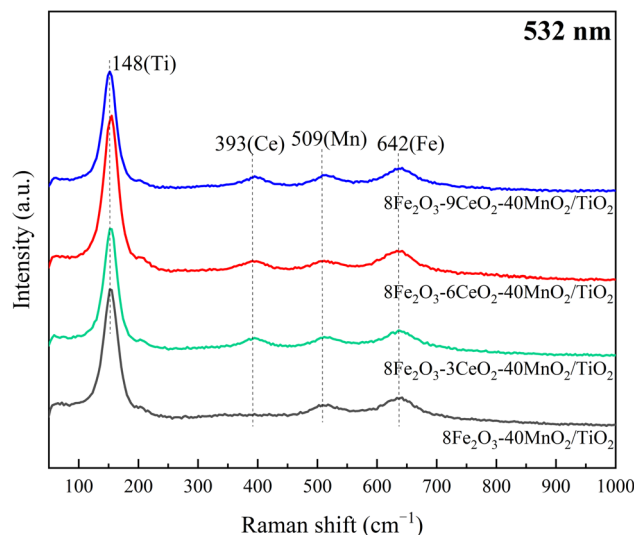
Fig. 8 Raman spectra of the $8Fe_2O_3-yCeO_2-40MnO_2/TiO_2$ catalysts at 532 nm.

3.4 Particle size analysis of the catalysts

The particle size of SCR denitrification catalysts is an important factor affecting their catalytic activity. Generally, the smaller the particle size of a catalyst, the larger its specific surface area and the greater its contact area with NO_x, NH_3, and other components in flue gas, resulting in more reaction sites, which can significantly enhance the rate and efficiency of the denitrification reaction. Particle size analysis was conducted on the $8Fe_2O_3-yCeO_2-40MnO_2/TiO_2$ catalysts with different amounts of added CeO_2, and the results are shown in Fig. 9. From Fig. 9, it can be seen that the particle size distribution of the catalysts is not uniform. As the amount of CeO_2 added increases, the number of particles with a size less than 10 μm significantly increases, while there is no significant change in the D90 particle size. The $8Fe_2O_3-6CeO_2-40MnO_2/TiO_2$ catalyst has the finest particles with a size of less than 45 μm, indicating that the addition of 6% CeO_2 leads to refinement of the particles of the catalyst, which is consistent with the BET results and is beneficial for the NH_3-SCR reaction.

3.5 Acidic site distribution of the catalysts

In the NH_3-SCR reaction, the adsorption of NH_3 at the active sites on the surface of the catalyst is the primary reaction. This can take two forms: one in which NH_3 is adsorbed at Brønsted acid sites to form NH_4^+, and another in which NH_3 is adsorbed at Lewis acid sites to form coordinatively bound NH_3 species. The key to Lewis acid sites is the "electron-deficient center", and there are unfilled electronic orbitals (such as d-orbitals of metal ions and p-orbitals of non-metal atoms) in the support that can accept lone pair electrons from base molecules to form coordination bonds. The core of this structural model is "the composition of electron-deficient center atoms and their electronic states". The key to Brønsted acid sites is the "weak interaction between protons and the support", whereby protons (H^+) can bind to negatively charged groups on the support

through hydrogen bonds or coordination bonds, and can dissociate and transfer to base molecules (such as NH_3 and pyridine) under the reaction conditions. This structural model must meet two conditions: (1) the support must have groups that can stably hold negative charges; (2) the H^+ must be able to dissociate after binding. Therefore, it is necessary to study the acid density, acid strength, and acid strength distribution on the surface of catalysts.[22] The $8Fe_2O_3-yCeO_2-40MnO_2/TiO_2$ catalyst was tested using NH_3-TPD, and the results are depicted in Fig. 10 and Table 3.

As can be seen from Fig. 10, each group of catalysts exhibits four obvious desorption peaks in the range from 50 to 800 °C. Among them, the desorption peak with the peak center between 25 and 200 °C corresponds to weak acid sites and is attributed to NH_3 adsorbed at Lewis acid sites or physically adsorbed NH_3; the desorption peak with the peak center between 200 and 400 °C corresponds to medium-strong acid sites and is attributed to NH_3 adsorbed at Lewis acid sites. The desorption peak with the peak center above 400 °C corresponds to strong acid sites and is attributed to NH_3 adsorbed at Brønsted acid sites.[23] As the content of CeO_2 increases, all of the desorption peaks of the catalyst shift toward lower temperatures, which indicates that the NH_3 adsorption capacity of the acidic sites on the surface in the low-temperature zone is enhanced, thereby improving the low-temperature denitration capacity of the catalyst. As shown in Table 3, when the content of CeO_2 is increased to 5%, the adsorption of NH_3 at weak acid sites, medium-strong acid sites, and strong acid sites on the surface of the catalyst increases to a certain extent, indicating that the Ce–O–Ce and Ce=O species in CeO_2 provide part of the Lewis and Brønsted acid sites for the catalyst.

3.6 Redox performance of the catalysts

In the NH_3-SCR reaction, the redox performance of the catalyst is essential to the denitration reaction cycle. H_2-TPR is an effective method for evaluating the reduction performance of NH_3-SCR catalysts. The $8Fe_2O_3-yCeO_2-40MnO_2/TiO_2$ catalysts were characterized by H_2-TPR, and the results are presented in Fig. 11 and Table 4.

As shown in Fig. 11, three reduction peaks appeared in each catalyst sample. Among them, the reduction peak at 250–350 °C corresponds to the reduction of $Fe^{3+} \rightarrow Fe^{2+}$; the reduction peak at 350–520 °C corresponds to the reduction of $Mn^{4+} \rightarrow Mn^{3+}$; and the reduction peak at 520–800 °C corresponds to the reduction of $Ce^{4+} \rightarrow Ce^{3+}$.[24-26] With the increase in CeO_2 content, most of the reduction peaks shift toward lower temperatures, indicating a decrease in the reduction temperature of the catalyst. This suggests that the surface chemical adsorption of oxygen is enhanced, which is conducive to the reduction of surface species. When the CeO_2 content is increased from 3% to 6%, the $Mn^{4+} \rightarrow Mn^{3+}$ reduction peak area decreases. The main reason for this is that there is an interaction between CeO_2 and MnO_2, $Ce^{3+} + Mn^{4+} \leftrightarrow Ce^{4+} + Mn^{3+}$, which makes it more difficult for some Mn^{4+} to be directly reduced. From the perspective of H_2 consumption (Table 4), the H_2 consumption of the $8Fe_2O_3-6CeO_2-40MnO_2/TiO_2$ catalyst
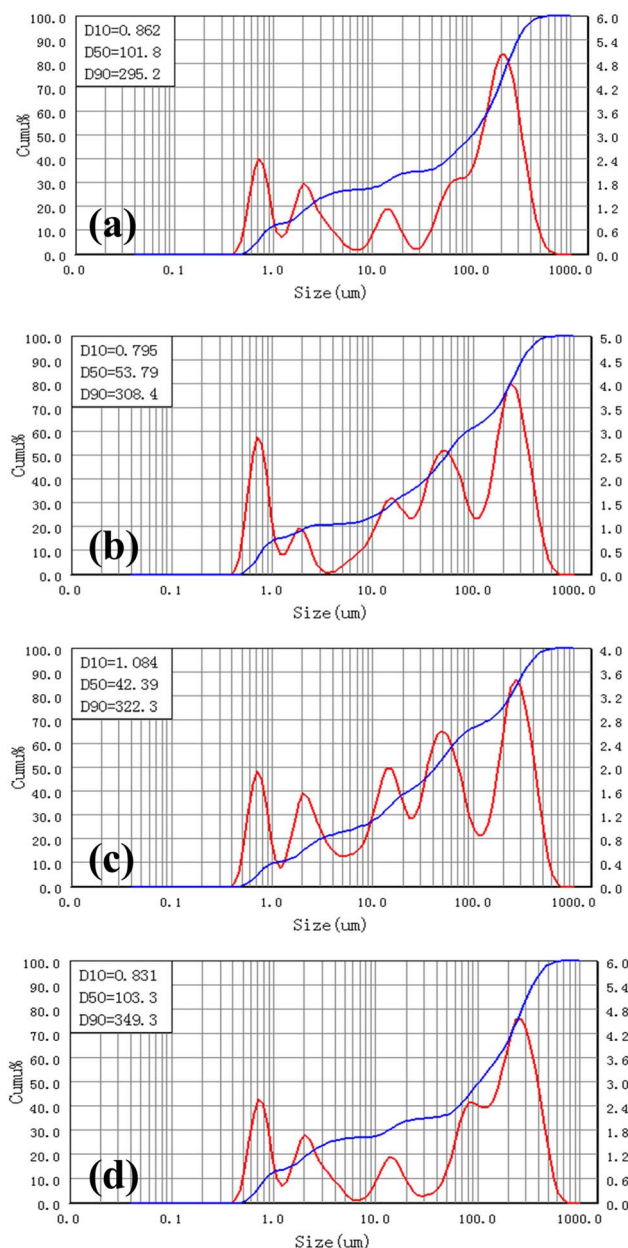
Fig. 9 Particle size analysis of the $8Fe_2O_3–yCeO_2–40MnO_2/TiO_2$ catalysts: (a) $8Fe_2O_3–40MnO_2/TiO_2$; (b) $8Fe_2O_3–3CeO_2–40MnO_2/TiO_2$; (c) $8Fe_2O_3–6CeO_2–40MnO_2/TiO_2$; and (d) $8Fe_2O_3–9CeO_2–40MnO_2/TiO_2$.

during the entire reduction process is increased significantly compared to that of the other catalysts, indicating that an appropriate CeO_2 content can enhance the overall reducibility of the catalyst, which is beneficial for promoting the NH$_3$-SCR reaction.

3.7 Catalytic mechanism analysis of the $8Fe_2O_3–6CeO_2–40MnO_2/TiO_2$ catalysts

The above analysis indicates that the catalytic activity of the $8Fe_2O_3–yCeO_2–40MnO_2/TiO_2$ catalysts is influenced by a variety of factors, and that one of the main reasons is the variation in acidic sites. The SCR reaction is a heterogeneous gas–solid

reaction catalyzed by a solid catalyst, which requires the catalyst to have sufficient active sites to adsorb the reaction gases. In order to study the changes in the adsorption characteristics of the $8Fe_2O_3–6CeO_2–40MnO_2/TiO_2$ catalyst during the low-temperature NH$_3$-SCR reaction and to explore the catalytic reaction mechanism on the catalyst surface, *in situ* DRIFTS was used to investigate the interaction between the reaction gases (NH$_3$ and NO) and the catalyst surface.

3.7.1 Adsorption of NH$_3$. In order to further clarify the properties of the NH$_3$(ad) species on the surface of the $8Fe_2O_3–6CeO_2–40MnO_2/TiO_2$ catalyst, *in situ* DRIFTS of NH$_3$ adsorption at different temperatures was conducted, and the results are shown in Fig. 12. Based on the spectrum of the $8Fe_2O_3–6CeO_2–40MnO_2/TiO_2$ catalyst, the bands that appear at 1768 cm^{-1}, 1603 cm^{-1}, 1342 cm^{-1}, and 1141 cm^{-1} correspond to NH$_3$ molecules coordinated to Lewis acid sites, while the band at 1420 cm^{-1} corresponds to NH$_4^+$ ions adsorbed at Brønsted acid sites.[27,28] As the temperature increases, the intensity of the absorption peaks associated with each acid site decreases due to the desorption and decomposition of adsorbed NH$_3$. Comparatively, the absorption peaks corresponding to the Brønsted acid sites weaken more rapidly, indicating that the Lewis acid sites have higher thermal stability than the Brønsted acid sites. Therefore, at low temperatures, NH$_3$ adsorption in the catalytic reaction involves both Lewis and Brønsted acid sites, whereas at high temperatures, NH$_3$ adsorption mainly occurs at Lewis acid sites.

3.7.2 Co-adsorption of NO + O$_2$. To understand the microscopic process of the NH$_3$-SCR reaction on the $8Fe_2O_3–6CeO_2–40MnO_2/TiO_2$ catalyst, it is necessary to distinguish the adsorbent species on the surface of the catalyst. Therefore, an *in situ* NO + O$_2$ co-adsorption experiment was carried out on the $8Fe_2O_3–6CeO_2–40MnO_2/TiO_2$ catalyst, and the results are shown in Fig. 13. The $8Fe_2O_3–6CeO_2–40MnO_2/TiO_2$ catalyst was exposed to a NO + O$_2$ gas mixture (500 ppm NO + 5% O$_2$, N$_2$ balance) at room temperature, and multiple infrared vibration signal peaks appeared between 1000 and 2000 cm^{-1}. Among them, the bands located at 1408 cm^{-1} and 1593 cm^{-1} can be attributed to bidentate nitrates; the band located at 1153 cm^{-1} is related to monodentate nitrates; the band located at 1342 cm^{-1} corresponds to M–NO$_2$ nitro compounds; the band located at 1615 cm^{-1} corresponds to adsorbed NO$_2$; and the band located at 1749 cm^{-1} corresponds to the physical adsorption of NO$_2$.[29,30] As can be seen from Fig. 11, as the temperature rises, the intensity of the absorption peaks corresponding to monodentate nitrate (1153 cm^{-1}) gradually decreases with increasing temperature, while the bidentate nitrate absorption peaks (1408 cm^{-1} and 1593 cm^{-1}) appear at lower temperatures and are not easily decomposed. This is due to the low thermal stability of the monodentate nitrate and a certain degree of desorption on the surface of the catalyst at high temperatures, and is consistent with the fact that bidentate nitrates are more thermally stable than monodentate nitrates. The peak intensity corresponding to the adsorbed NO$_2$ (1615 cm^{-1}) gradually decreases with increasing temperature, which is related to the effect of NO oxidation and the accelerated desorption of NO$_2$ after the temperature increase.
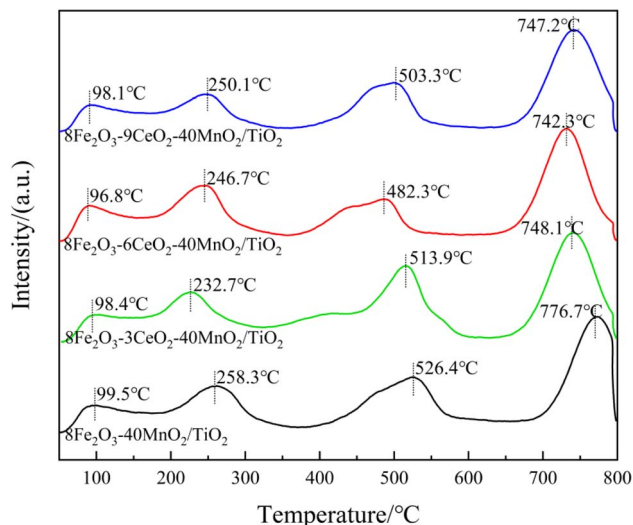
Fig. 10 NH$_3$-TPD patterns of the 8Fe$_2$O$_3$–yCeO$_2$–40MnO$_2$/TiO$_2$ catalysts.
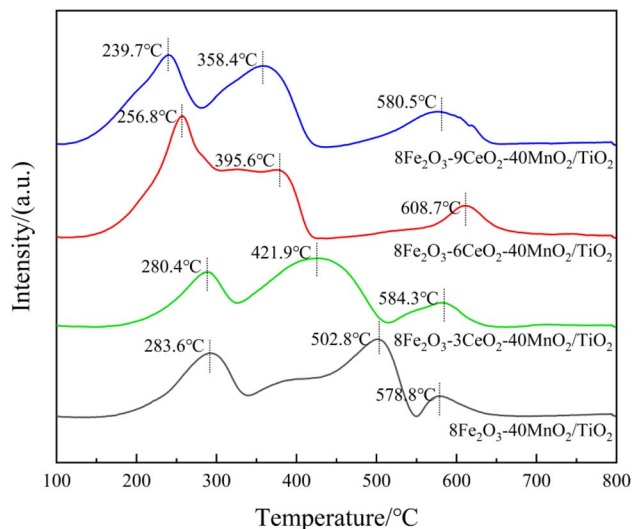
Fig. 11 H$_2$-TPR patterns of the 8Fe$_2$O$_3$–yCeO$_2$–40MnO$_2$/TiO$_2$ catalysts.

3.7.3 The microscopic reaction process of the catalyst. The 8Fe$_2$O$_3$–6CeO$_2$–40MnO$_2$/TiO$_2$ catalyst was pre-adsorbed with NH$_3$ and subjected to *in situ* NO + O$_2$ co-adsorption tests in order to explore the microscopic process of the NH$_3$-SCR reaction on the 8Fe$_2$O$_3$–6CeO$_2$–40MnO$_2$/TiO$_2$ catalyst at 250 °C. The results are shown in Fig. 14. At 250 °C, when NH$_3$ adsorption was saturated, signals corresponding to Lewis acid sites (1165 cm^{-1}, 1352 cm^{-1}, and 1603 cm^{-1}) and Brønsted acid sites (1420 cm^{-1}) were observed. Then, the NH$_3$ gas supply was turned off, and a NO + O$_2$ gas mixture (500 ppm NO + 5% O$_2$, balanced with N$_2$) was introduced. The following phenomena were observed over time: after 20 minutes of NO + O$_2$ exposure, the signals related to NH$_3$ adsorption completely disappeared, indicating that almost all the NH$_3$ species adsorbed on the catalyst surface had participated in the reaction. Subsequently, absorption peaks corresponding to bidentate nitrates (1408 cm^{-1}), monodentate nitrates (1153 cm^{-1}), M–NO$_2$ nitro compounds (1342 cm^{-1}), and adsorbed NO$_2$ (1602 cm^{-1}) appeared. The intensity of the bidentate nitrate peak at 1408 cm^{-1} further increased with prolonged reaction time, likely due to the accumulation of bidentate nitrate species after the surface-adsorbed NH$_3$ species were fully consumed. These results indicate that the 8Fe$_2$O$_3$–6CeO$_2$–40MnO$_2$/TiO$_2$ catalyst can adsorb NO + O$_2$ and convert it into various nitrate species. These nitrate species then react with the NH$_3$ species previously adsorbed on the Lewis and Brønsted acid sites to complete the denitration reaction cycle. The NH$_3$-SCR reaction on the catalyst surface follows the L–H mechanism, as shown in eqn (3.1)–(3.9).[31]
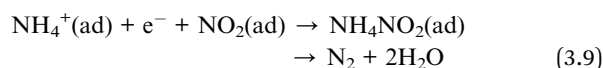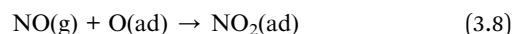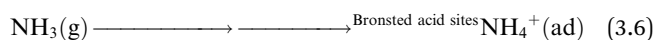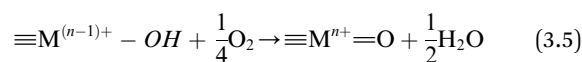
$$NH_3(g) \xrightarrow{\quad\quad\quad\quad\text{Lewis acid sites}\quad} NH_3(ad) \quad (3.1)$$

$$NO(g) \rightarrow NO(ad) \quad (3.2)$$

$$\equiv M^{n+}=O + NO(ad) \rightarrow \equiv M^{(n-1)+}-O-NO \quad (3.3)$$

$$M^{(n-1)+}-O-NO + NH_3(ad) \rightarrow \equiv M^{(n-1)+}-O-NO-NH_3 \rightarrow$$
$$\equiv M^{(n-1)+}-OH + N_2(g) + H_2O \quad (3.4)$$

$$\equiv M^{(n-1)+}-OH + \frac{1}{4}O_2 \rightarrow \equiv M^{n+}=O + \frac{1}{2}H_2O \quad (3.5)$$

$$NH_3(g) \xrightarrow{\quad\quad\quad\quad\text{Bronsted acid sites}\quad} NH_4^+(ad) \quad (3.6)$$

$$O_2(g) \rightarrow 2O(ad) \quad (3.7)$$

$$NO(g) + O(ad) \rightarrow NO_2(ad) \quad (3.8)$$

$$NH_4^+(ad) + e^- + NO_2(ad) \rightarrow NH_4NO_2(ad)$$
$$\rightarrow N_2 + 2H_2O \quad (3.9)$$
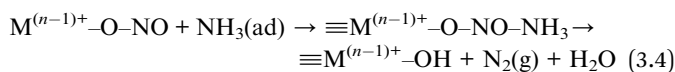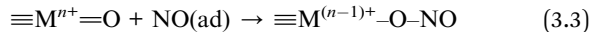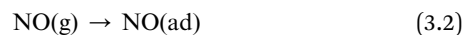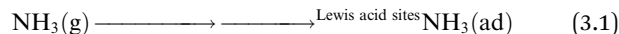
Table 3 NH$_3$ adsorption capacity of the 8Fe$_2$O$_3$–yCeO$_2$–40MnO$_2$/TiO$_2$ catalysts

Catalyst	NH$_3$ adsorption at the weak acid sites/µmol g^{-1}	NH$_3$ adsorption at the medium-strong acid sites/µmol g^{-1}	NH$_3$ adsorption at the strong acid sites/µmol g^{-1}
8Fe$_2$O$_3$–40MnO$_2$/TiO$_2$	175.46	295.37	983.54
8Fe$_2$O$_3$–3CeO$_2$–40MnO$_2$/TiO$_2$	168.72	247.18	1022.35
8Fe$_2$O$_3$–6CeO$_2$–40MnO$_2$/TiO$_2$	187.15	318.66	1108.59
8Fe$_2$O$_3$–9CeO$_2$–40MnO$_2$/TiO$_2$	182.52	256.35	1107.28

Table 4 H$_2$ consumption of the 8Fe$_2$O$_3$–yCeO$_2$–40MnO$_2$/TiO$_2$ catalysts

Catalyst	Fe^{3+} → Fe^{2+} H$_2$ consumption/mmol g^{-1}	Mn^{4+} → Mn^{3+} H$_2$ consumption/mmol g^{-1}	Ce^{4+} → Ce^{3+} H$_2$ consumption/mmol g^{-1}	Total consumption of H$_2$/mmol g^{-1}
8Fe$_2$O$_3$–40MnO$_2$/TiO$_2$	2.65	4.65	0.83	8.13
8Fe$_2$O$_3$–3CeO$_2$– 40MnO$_2$/TiO$_2$	2.83	5.94	1.01	9.78
8Fe$_2$O$_3$–6CeO$_2$– 40MnO$_2$/TiO$_2$	4.18	5.73	1.34	11.25
8Fe$_2$O$_3$–9CeO$_2$– 40MnO$_2$/TiO$_2$	3.23	4.71	2.46	10.40
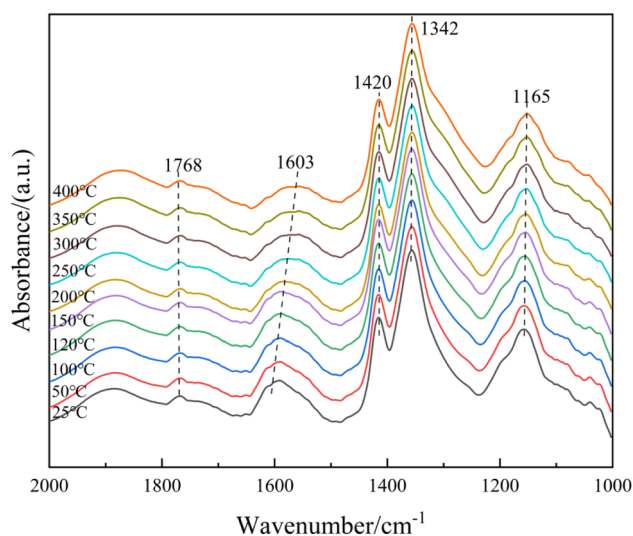
Fig. 12 *In situ* DRIFTS spectra of NH$_3$ adsorption on the 8Fe$_2$O$_3$– 6CeO$_2$–40MnO$_2$/TiO$_2$ catalyst.

Additionally, the 8Fe$_2$O$_3$–6CeO$_2$–40MnO$_2$/TiO$_2$ catalyst was pre-adsorbed with NO + O$_2$ and subjected to *in situ* NH$_3$ adsorption at 250 °C, as shown in Fig. 15. When the 8Fe$_2$O$_3$–

6CeO$_2$–40MnO$_2$/TiO$_2$ catalyst adsorbed NO + O$_2$ at 250 °C and reached saturation, the absorption peaks of bidentate nitrate (1408 cm^{-1}), monodentate nitrate (1153 cm^{-1}), bridged nitrate (1269 cm^{-1}), M–NO$_2$ nitro compounds (1342 cm^{-1}), and adsorbed NO$_2$ (1602 cm^{-1}) were detected. Then, the NO + O$_2$ gas mixture was turned off and NH$_3$ gas was introduced. Over time, the following phenomena occurred: after the NH$_3$ gas had been introduced for 10 minutes, the signals related to the adsorption of NO + O$_2$ disappeared, indicating that the nitrate species adsorbed on the surface of the catalyst had fully participated in the reaction. After 10 minutes, the Lewis acid sites (1165 cm^{-1}, 1352 cm^{-1}, and 1603 cm^{-1}) and Brønsted acid sites (1269 cm^{-1}, 1420 cm^{-1}, and 1530 cm^{-1}) had adsorbed NH$_3$ species, giving rise to the corresponding absorption peaks. The intensity of the absorption peaks did not change significantly with extension of the reaction time, indicating that the reaction is complete at this point. The above results show that the NO$_x$ species adsorbed on the surface of the 8Fe$_2$O$_3$–6CeO$_2$–40MnO$_2$/TiO$_2$ catalyst can react with gaseous NH$_3$ molecules, indicating that the NH$_3$-SCR reaction on the catalyst surface also follows the E–R mechanism as shown in reaction eqn (3.10)–(3.14).[31] Combining the information in Fig. 12 and 13, it can be concluded that the NH$_3$-SCR reaction on the surface of the
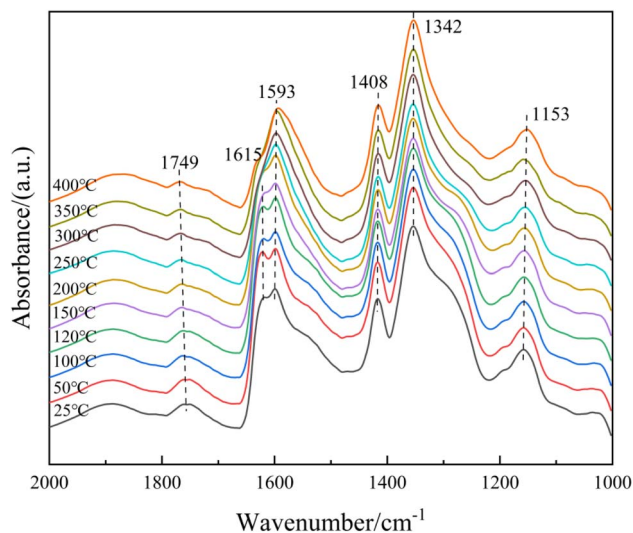
Fig. 13 *In situ* DRIFTS spectra of NO + O$_2$ adsorption on the 8Fe$_2$O$_3$– 6CeO$_2$–40MnO$_2$/TiO$_2$ catalyst.
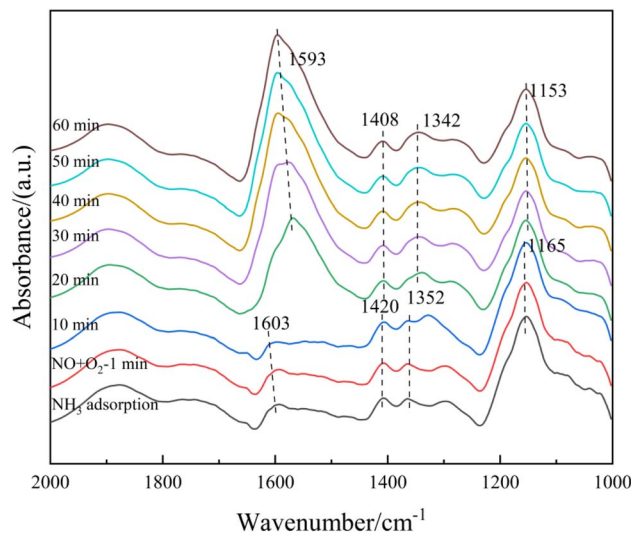
Fig. 14 *In situ* DRIFTS spectra of NO + O$_2$ adsorption on the 8Fe$_2$O$_3$– 6CeO$_2$–40MnO$_2$/TiO$_2$ catalyst with pre-adsorption of NH$_3$.

$8Fe_2O_3–6CeO_2–40MnO_2/TiO_2$ catalyst follows both the L–H and E–R mechanisms, with the L–H mechanism being dominant.

$$NH_3(g) \rightarrow NH_3(ad) \tag{3.10}$$

$$NH_3(ad) + M^{n+}=O \rightarrow NH_2(ad) + M^{(n-1)+}–O–H \tag{3.11}$$

$$NH_2(ad) + M^{n+}=O \rightarrow NH(ad) + M^{(n-1)+}–O–H \tag{3.12}$$

$$NH_2(ad) + NO(g) \rightarrow N_2 + H_2O \tag{3.13}$$

$$NH(ad) + NO(g) \rightarrow N_2O + H^+ \tag{3.14}$$
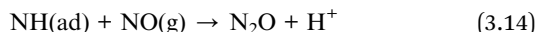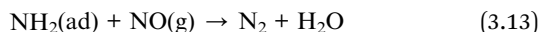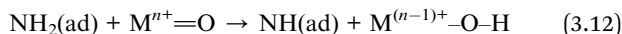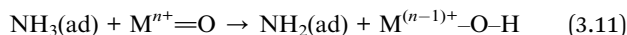
3.8 Catalytic activity of the $8Fe_2O_3–yCeO_2–40MnO_2/TiO_2$ catalysts

3.8.1 Denitration performance of the $8Fe_2O_3–yCeO_2–40MnO_2/TiO_2$ catalysts. The results of the denitration performance tests of the $8Fe_2O_3–yCeO_2–40MnO_2/TiO_2$ catalysts with different CeO_2 contents are shown in Fig. 16(a). The denitration performance of the catalyst with no added CeO_2 was the worst. The temperature at which its denitration efficiency reached 80% was 121 °C, and the temperature ranges for 80% and 90% denitration efficiencies were 121–385 °C and 133–355 °C, respectively. As the CeO_2 content was increased, the denitration performance of the catalyst also improved. When the content was increased to 6%, the catalyst showed the best denitration performance. The initial temperature at which it achieved 80% denitration efficiency was reduced to 115 °C, the temperature ranges for denitration efficiencies greater than 80% and 90% were widened to 115–425 °C and 129–390 °C, respectively, with the highest denitration efficiency reaching 99.17%. When the CeO_2 content was further increased to 9%, the denitration performance of the catalyst began to decline.

The N_2 selectivity of the $8Fe_2O_3–yCeO_2–40MnO_2/TiO_2$ catalysts is shown in Fig. 16(b). At temperatures below 200 °C, all the catalyst groups maintain 100% N_2 selectivity. As the temperature rises, the N_2 selectivity shows a downward trend for all the catalysts, indicating that some NH_3 is over-oxidized at higher temperatures and the by-product N_2O begins to form. Among them, the $8Fe_2O_3–6CeO_2–40MnO_2/TiO_2$ catalyst exhibits the best N_2 selectivity, with the lowest rate of decline, maintaining a selectivity of 80.3% at 450 °C. At this temperature, the N_2 selectivity of the other catalysts drops below 78%.

3.8.2 Anti-SO_2 and anti-H_2O properties of the $8Fe_2O_3–yCeO_2–40MnO_2/TiO_2$ catalysts. The results of the SO_2 and H_2O resistance tests of the $8Fe_2O_3–yCeO_2–40MnO_2/TiO_2$ catalysts are shown in Fig. 17. From the above denitration performance test results, it can be seen that the denitration efficiency of each group of catalysts reaches its maximum value near 200 °C and tends to stabilize, indicating that the denitration performance of the catalysts is best at this temperature. As shown in Fig. 17(a), after each group of catalysts was operated stably at 200 °C for 6 hours, 60 ppm SO_2 was introduced into the simulated flue gas. At this time, the denitration efficiency of each group of catalysts decreased significantly to a certain value and then stabilized. After 18 hours, the introduction of SO_2 was
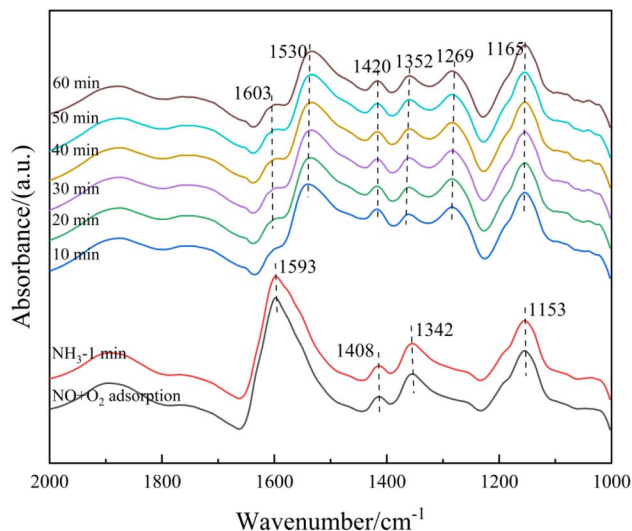

Fig. 15 *In situ* DRIFTS spectra of NH_3 adsorption on the $8Fe_2O_3–6CeO_2–40MnO_2/TiO_2$ catalyst with pre-adsorption of NO + O_2.

stopped. Subsequently, the denitration efficiency gradually recovered to a certain value and remained stable, but remained lower than the initial value, indicating that the effect of SO_2 on the denitration performance of the catalyst is irreversible. Among the catalysts, the $8Fe_2O_3–40MnO_2/TiO_2$ catalyst is most affected by SO_2, followed by the $8Fe_2O_3–3CeO_2–40MnO_2/TiO_2$ catalyst and the $8Fe_2O_3–9CeO_2–40MnO_2/TiO_2$ catalyst. The $8Fe_2O_3–6CeO_2–40MnO_2/TiO_2$ catalyst was least affected and almost recovered to the level before the introduction of SO_2 after the SO_2 was removed. The improved denitration efficiency is mainly due to the fact that an appropriate amount of CeO_2 can inhibit the generation of $(NH_4)_2SO_4$ and reduce the stability of $(NH_4)_2SO_4$ and NH_4HSO_4, thereby improving the resistance of the catalyst to SO_2.

As shown in Fig. 17(b), after constant temperature denitration at 200 °C for 6 hours, 60 ppm SO_2 and water vapor with a volume fraction of 5% were introduced into the mixed flue gas simultaneously. The denitration efficiencies of the catalysts with CeO_2 contents of 1%, 3%, 5%, and 7% decreased to 74.5%, 79.5%, 81.6%, and 80.1%, respectively, and then gradually stabilized. After the reaction had been carried out for 18 hours, the introduction of SO_2 and H_2O was stopped. The denitration efficiency improved to some extent as the reaction continued, although it failed to recover to the value prior to the introduction of SO_2 and water vapor. Among the catalysts, the $8Fe_2O_3–40MnO_2/TiO_2$ catalyst was most affected by SO_2 and H_2O. The main reason is that when the CeO_2 content is low, it is difficult for the catalyst to inhibit its own sulfation, and H_2O competes with NH_3 for adsorption on the surface of the catalyst, thereby affecting the surface adsorption performance of the catalyst. The $8Fe_2O_3–6CeO_2–40MnO_2/TiO_2$ catalyst maintained a denitration efficiency of more than 80% after the introduction of SO_2 and H_2O. After the introduction of SO_2 and H_2O was stopped, its denitration efficiency gradually increased to greater than 90%, showing excellent anti-SO_2 and anti-H_2O properties.[32]
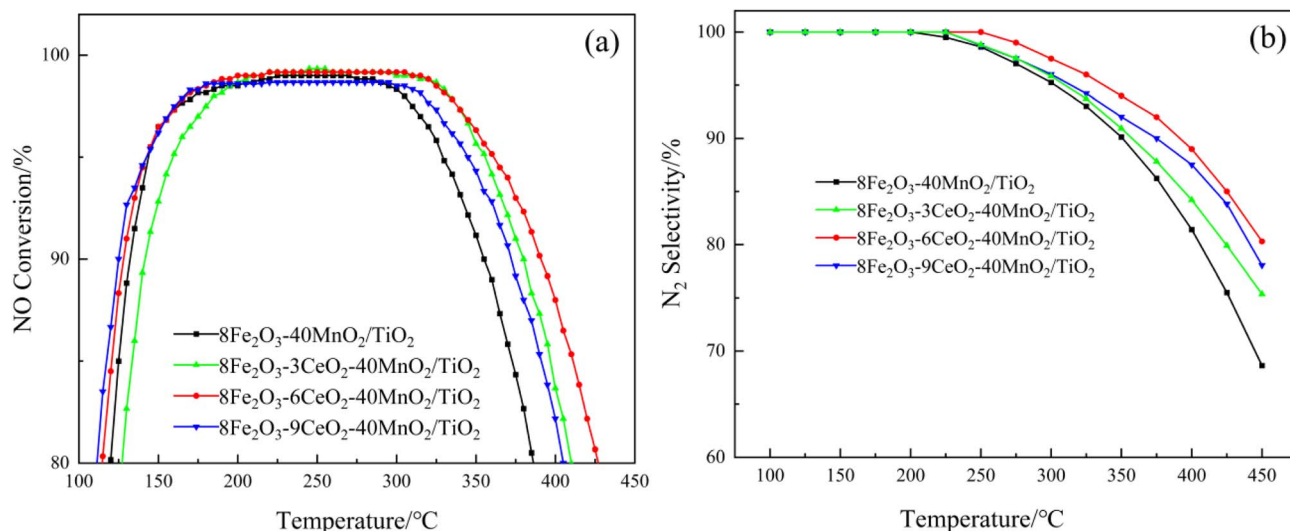
Fig. 16 Denitration performance of the $8Fe_2O_3-yCeO_2-40MnO_2/TiO_2$ catalysts: (a) NO conversion; and (b) N_2 selectivity.

3.8.3 Kinetic analysis of the $8Fe_2O_3-yCeO_2-40MnO_2/TiO_2$ catalysts. To further investigate the influence of rare earth modification on the catalytic reaction rate of $Fe_2O_3-MnO_2/TiO_2$, the dynamics of the denitration reaction were studied. Differences in the apparent activation energy of the catalytic reaction can help to determine the different catalytic paths and the adsorption and desorption behaviors of species on the catalyst surface.[33] The calculation method for the reaction rate constant is shown in eqn (3.15):[34]

$$k = -\frac{V}{W}\ln(1 - X) \qquad (3.15)$$

where k represents the reaction rate constant (cm^3 g^{-1} s^{-1}), V is the gas flow rate (cm^3 s^{-1}), W is the catalyst mass (g), and X is the NO conversion rate. The value of k is calculated using eqn (3.15). Subsequently, based on the R and T values, the Arrhenius linear diagram is constructed through three-point linear fitting.

$$\ln k = \ln A - E_a/(RT) \qquad (3.16)$$

where A refers to the pre-exponential factor (cm^3 g^{-1} s^{-1}), E_a represents the apparent activation energy (J mol^{-1}), R is the universal gas constant, which has a value of 8.314 (J K^{-1} mol^{-1}), and T is the reaction temperature in kelvin (K). In addition, $1/T$ is used as the abscissa, and the natural logarithm of the reaction rate, $\ln k$, is plotted as the ordinate. There is a linear relationship between $1/T$ and $\ln k$, and the reaction activation energy E_a can be obtained through linear regression.

Combined with the denitration performance test results of the catalysts, the denitration reaction kinetics of the $8Fe_2O_3-yCeO_2-40MnO_2/TiO_2$ catalyst were studied using eqn (3.15) and (3.16). The results are shown in Fig. 18. From eqn (3.16), it can be seen that $\ln k$ has a linear relationship with T^{-1}. The smaller the absolute value of the slope, the smaller the reaction activation energy E_a, and the more easily the denitration reaction proceeds. The absolute value of the slope of the $8Fe_2O_3-6CeO_2-40MnO_2/TiO_2$ catalyst is the smallest; thus, the catalyst with 5%

added CeO_2 has the smallest activation energy, E_a = 55.78 kJ mol^{-1}. In addition, as the reaction temperature increases, the reaction rate of the catalyst also increases. At a given temperature, the reaction rates follow the order $8Fe_2O_3-6CeO_2-40MnO_2/TiO_2$ > $8Fe_2O_3-9CeO_2-40MnO_2/TiO_2$ > $8Fe_2O_3-3CeO_2-40MnO_2/TiO_2$ > $8Fe_2O_3-40MnO_2/TiO_2$, which is consistent with the denitration performance test results shown in Fig. 16.

4 Conclusions

In this study, a new type of catalyst, $8Fe_2O_3-yCeO_2-40MnO_2/TiO_2$, which was modified using the rare earth oxide (CeO_2) with Fe–Mn/TiO_2 catalyst as the main body, was investigated. The denitration properties and reaction dynamics of NH_3 reducing NO were also analyzed. The results show that the $8Fe_2O_3-6CeO_2-40MnO_2/TiO_2$ catalyst modified with 6% CeO_2 exhibits the best denitration performance. The catalyst has the smallest reaction activation energy (E_a = 55.78 kJ mol^{-1}). Its denitration efficiency exceeds 80% in the temperature range from 115 to 425 °C and 90% in the range from 129 to 390 °C. The highest denitration efficiency (99.17%) is achieved within the temperature range of 220–305 °C, and the catalyst demonstrates good N_2 selectivity as well as strong anti-SO_2 and anti-H_2O performance. The $8Fe_2O_3-yCeO_2-40MnO_2/TiO_2$ catalyst was characterized using XRD, BET, SEM, TEM, XPS, TPR, and TPD techniques, and the effects of the addition of CeO_2 on the structure and morphology, surface characteristics, acid site distribution, and redox properties of the catalyst were investigated. The addition of 6% CeO_2 promotes lattice shrinkage of TiO_2, improves the dispersion of TiO_2, and increases the specific surface area of the catalyst. The chemical adsorption of oxygen and low-valence metal ions (Fe^{2+}/Ce^{3+}) on the catalyst surface are enhanced, providing more oxygen vacancies and surface active sites for the NH_3-SCR reaction. At the same time, the redox capacity of the catalyst is enhanced, which facilitates
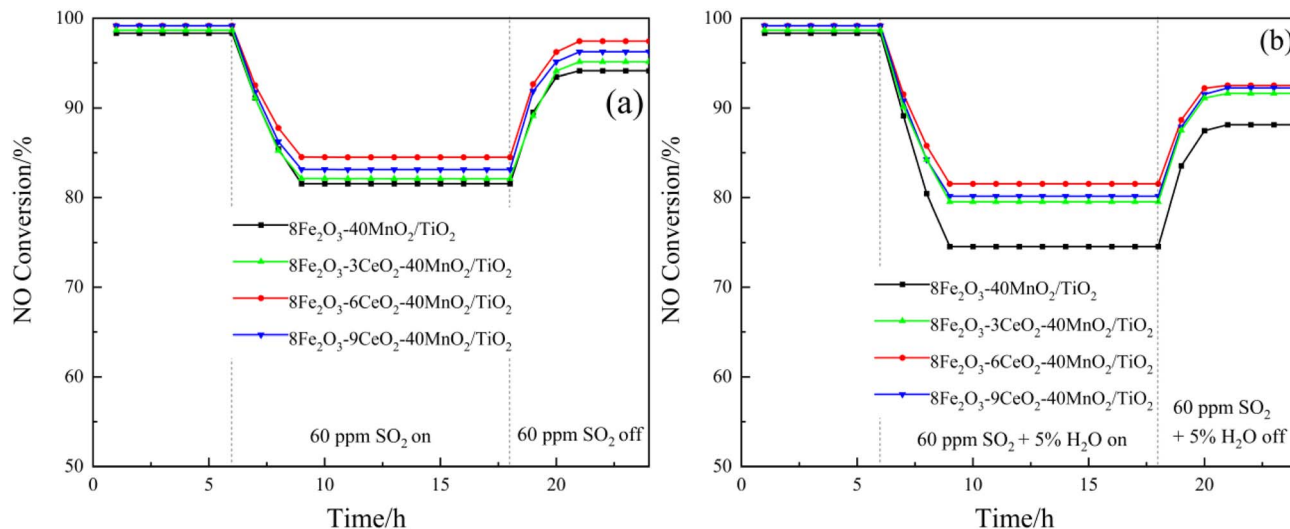
Fig. 17 SO$_2$ and H$_2$O resistance of the 8Fe$_2$O$_3$–yCeO$_2$–40MnO$_2$/TiO$_2$ catalysts: (a) SO$_2$; and (b) SO$_2$ and H$_2$O.
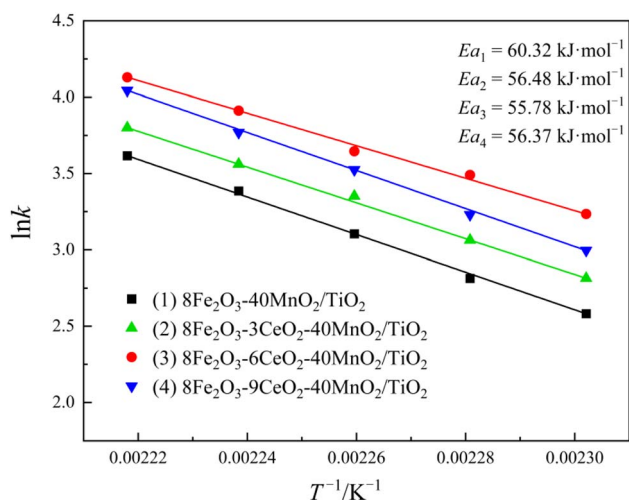
Fig. 18 Kinetic diagrams of the 8Fe$_2$O$_3$–yCeO$_2$–40MnO$_2$/TiO$_2$ catalysts.

the NH$_3$-SCR reaction. The addition of CeO$_2$ promotes the formation of weak and medium-strong acid sites on the catalyst surface, significantly improving the low-temperature denitration capacity of the Fe–Mn/TiO$_2$ catalyst. *In situ* DRIFTS results indicate that the NH$_3$-SCR reaction on the surface of the 8Fe$_2$O$_3$–6CeO$_2$–40MnO$_2$/TiO$_2$ catalyst follows both L–H and E–R mechanisms, with the L–H mechanism being dominant.

Conflicts of interest

There are no conflicts to declare.

Data availability

All relevant data are within the paper.

References

1 F. Zheng, C. Liu, X. Ma, Z. Zhou and J. Lu, *Fuel Process. Technol.*, 2023, **247**, 107773.

2 T. Boningari and P. G. Smirniotis, *Curr. Opin. Chem. Eng.*, 2016, **13**, 133–141.

3 E. D. Park, *Molecules*, 2024, **29**, 4506.

4 Z. Fan, J.-W. Shi, C. Niu, B. Wang, C. He and Y. Cheng, *Chem. Eng. J.*, 2020, **398**, 125572.

5 J.-K. Lai and I. E. Wachs, *ACS Catal.*, 2018, **8**, 6537–6551.

6 L. Han, S. Cai, M. Gao, J. Hasegawa, P. Wang, J. Zhang, L. Shi and D. Zhang, *Chem. Rev.*, 2019, **119**, 10916–10976.

7 Q. Liu, J. Yang, M. Luo, Z. Yang and Q. Zhao, *Catal. Lett.*, 2021, **151**, 966–979.

8 J. Mu, X. Li, W. Sun, S. Fan, X. Wang, L. Wang, M. Qin, G. Gan, Z. Yin and D. Zhang, *Ind. Eng. Chem. Res.*, 2018, **57**, 10159–10169.

9 M. N. Khan, L. Han, P. Wang, J. He, B. Yang, T. Yan, L. Shi and D. Zhang, *Chem. Eng. J.*, 2020, **397**, 125535.

10 G. Zhai, Z. Han, H. Du, Y. Gao and X. Pan, *Environ. Sci. Pollut. Res.*, 2022, **29**, 17295–17308.

11 Z. Liu, C. Chen, J. Zhao, L. Yang, K. Sun, L. Zeng, Y. Pan, Y. Liu and C. Liu, *Chem. Eng. J.*, 2020, **379**, 122288.

12 C. Gao, J.-W. Shi, Z. Fan, B. Wang, Y. Wang, C. He, X. Wang, J. Li and C. Niu, *Appl. Catal., A*, 2018, **564**, 102–112.

13 J. Huang, H. Huang, H. Jiang and L. Liu, *Catal. Today*, 2019, **332**, 49–58.

14 L. Xu, X.-S. Li, M. Crocker, Z.-S. Zhang, A.-M. Zhu and C. Shi, *J. Mol. Catal. A: Chem.*, 2013, **378**, 82–90.

15 J. Rong, W. Zhao, W. Luo, K. Kang, L. Long, Y. Chen and X. Yao, *J. Rare Earths*, 2023, **41**, 1323–1335.

16 B. Shen, T. Liu, N. Zhao, X. Yang and L. Deng, *J. Environ. Sci.*, 2010, **22**, 1447–1454.

17 T. Zhu, X. Zhang, W. Bian, Y. Han, T. Liu and H. Liu, *Catalysts*, 2020, **10**, 135.

18 S. M. Lee, K. H. Park and S. C. Hong, *Chem. Eng. J.*, 2012, **195–196**, 323–331.

19 S. Ma, X. Zhao, Y. Li, T. Zhang, F. Yuan, X. Niu and Y. Zhu, *Appl. Catal., B*, 2019, **248**, 226–238.

20 J. Xu, H. Yu, C. Zhang, F. Guo and J. Xie, *New J. Chem.*, 2019, **43**, 3996–4007.

21 H. Vidal, J. Kašpar, M. Pijolat, G. Colon, S. Bernal, A. Cordón, V. Perrichon and F. Fally, *Appl. Catal., B*, 2000, **27**, 49–63.

22 D. H. Kim, Y. J. Park, K.-Y. Lee, H. P. Ha and D. W. Kwon, *Appl. Catal., A*, 2022, **643**, 118770.

23 C. Yang, J. Yang, Q. Jiao, D. Zhao, Y. Zhang, L. Liu, G. Hu and J. Li, *Ceram. Int.*, 2020, **46**, 4394–4401.

24 T. Doan, P. Dam, K. Nguyen, T. H. Vuong, M. T. Le and T. H. Pham, *Catalysts*, 2020, **10**, 321.

25 K. Cheng, J. Liu, T. Zhang, J. Li, Z. Zhao, Y. Wei, G. Jiang and A. Duan, *J. Environ. Sci.*, 2014, **26**, 2106–2113.

26 A. Stahl, Z. Wang, T. Schwämmle, J. Ke and X. Li, *Catalysts*, 2017, **7**, 71.

27 C. Sun, H. Liu, W. Chen, D. Chen, S. Yu, A. Liu, L. Dong and S. Feng, *Chem. Eng. J.*, 2018, **347**, 27–40.

28 Z. Lian, F. Liu, H. He, X. Shi, J. Mo and Z. Wu, *Chem. Eng. J.*, 2014, **250**, 390–398.

29 Z. Liu, Y. Yi, S. Zhang, T. Zhu, J. Zhu and J. Wang, *Catal. Today*, 2013, **216**, 76–81.

30 B. Qin, R. Guo, L. Wei, X. Yin, T. Yin, J. Zhou and Z. Qiu, *J. Environ. Chem. Eng.*, 2022, **10**, 108564.

31 R. Guo, B. Qin, L. Wei, T. Yin, J. Zhou and W. Pan, *Phys. Chem. Chem. Phys.*, 2022, **24**, 6363–6382.

32 K. A. Michalow-Mauke, Y. Lu and K. Kowalski, *ACS Catal.*, 2015, **5**, 5657–5672.

33 L. Yan, Y. Liu, H. Hu, H. Li, L. Shi and D. Zhang, *ChemCatChem*, 2016, **8**, 2267–2278.

34 J.-W. Shi, Y. Wang, R. Duan, C. Gao, B. Wang, C. He and C. Niu, *Catal. Sci. Technol.*, 2019, **9**, 718–730.